

Tailored tunnel magnetoresistance response in three ultrathin chromium trihalides

Hyun Ho Kim^{1*}, Bowen Yang¹, Shangjie Tian², Chenghe Li², Guo-Xing Miao¹, Hechang Lei², and Adam W. Tsen^{1*}

¹*Institute for Quantum Computing, Department of Chemistry, Department of Physics and Astronomy, and Department of Electrical and Computer Engineering, University of Waterloo, Waterloo, Ontario N2L 3G1, Canada*

²*Department of Physics and Beijing Key Laboratory of Opto-electronic Functional Materials & Micro-Nano Devices, Renmin University of China, Beijing 100872, China*

*Correspondence to: hyun.kim@uwaterloo.ca, awtsen@uwaterloo.ca

Keywords: 2D magnetism, chromium trihalides, tunnel magnetoresistance, van der Waals heterostructures

Abstract

Materials that demonstrate large magnetoresistance have attracted significant interest for many decades. Recently, extremely large tunnel magnetoresistance (TMR) has been reported by several groups across ultrathin CrI₃ by exploiting the weak antiferromagnetic coupling between adjacent layers. Here, we report a comparative study of TMR in all three chromium trihalides (CrX₃, X= Cl, Br, or I) in the two-dimensional limit. As the materials exhibit different transition temperatures and interlayer magnetic ordering in the ground state, tunneling measurements allow for an easy determination of the field–temperature phase diagram for the three systems. By changing sample thickness and biasing conditions, we then demonstrate how to maximize and further tailor the TMR response at different temperatures for each material. In particular, near the magnetic transition temperature, TMR is non-saturating up to the highest fields measured for all three compounds owing to the large, field-induced exchange coupling.

Materials that show a substantial change in resistance in response to an applied magnetic field, or large magnetoresistance (MR), are generally rare but highly sought-after, both for fundamental interest as well as for potential applications in magnetic sensors and memory¹⁻⁶. In non-magnetic semimetals, such as WTe₂³ or MoTe₂⁷, extreme *positive* MR (10⁶% at 10T) can be achieved at low temperature due to both a balance of electron and hole carriers⁸⁻¹⁰ as well as their relatively high mobilities^{11,12}. The MR is further non-saturating up to the highest fields measured. In magnetic thin-films or perovskite manganites, respectively, giant (10³%)¹³ or colossal (10⁶%)¹⁴ *negative* MR can instead be achieved at higher temperatures. The former effect forms the basis of magnetic memory technology due to the low critical fields needed to saturate the MR.

The recent discoveries of 2D magnets¹⁵⁻¹⁷, such as CrI₃, provide a novel opportunity to explore large MR materials through the use of van der Waals heterostructures. Despite being insulating, electrons can tunnel through the CrI₃ layers in the ultrathin limit. Several groups have previously demonstrated negative tunnel magnetoresistance (TMR) as large as 10⁶% in graphene/CrI₃/graphene junctions under a 2T field at optimized biasing voltage¹⁸⁻²⁰. Here, as the antiferromagnetically coupled CrI₃ layers become polarized by the magnetic field²¹⁻²³, the tunneling current increases dramatically due to an electron spin-filtering effect²⁴. This result motivates a systematic study of TMR in the entire CrX₃ (X= I, Br, and Cl) family across bias, temperature, sample thickness, as well as contact material. For CrI₃ and CrCl₃ with antiferromagnetic (AFM) interlayer coupling, we observe the largest TMR in slightly thicker samples at low temperature, but which saturates at the critical polarizing field of 2T, while CrBr₃ samples with ferromagnetic (FM) interlayer coupling always show negligible TMR in the ground state. Near the transition temperature, however, all three materials demonstrate non-saturating TMR up to 14T. We interpret this effect as a field-induced splitting of the paramagnetic electron

bandstructure. Surprisingly, this splitting can be over 80% of the value in the ground state. Finally, using NbSe₂ with larger work function in place of graphene, we find that exchange splitting is much smaller for hole carriers in the valence band, consistent with theoretical expectations. Our results establish CrX₃ as a highly tunable platform to study TMR physics using relatively simple device geometries.

A schematic illustration of our devices is shown in the left panel of Fig. 1a and the detailed fabrication procedure can be found in the Methods section. In short, ultrathin CrI₃, CrBr₃, or CrCl₃ from 2 to 15 layers (L) is exfoliated in a nitrogen-filled glovebox and sandwiched between top and bottom few-layer graphene electrodes (Gr) with full encapsulation by hexagonal boron nitride (hBN) on both sides for sample protection. In the right panel of Fig. 1a, we show an optical image of such a CrI₃ device as an example. Our key findings can be summarized as a plot of TMR vs. thickness for each material measured at their “optimal” temperature, as shown in Fig. 1b. While their differences shall be explained in detail in the remaining sections, we note that the largest TMR response is generally observed in samples over 6L, and so we show main measurements on devices in this thickness regime.

We begin with transport behavior without magnetic field in order to confirm the ground-state magnetic properties of CrX₃. In Fig. 2, we show temperature-dependent I-V characteristics for few-layer devices incorporating the three different materials (CrI₃: 8L, CrBr₃: 8L, and CrCl₃: 15L). All tunnel junctions exhibit nonlinear current-voltage characteristics due to quantum mechanical tunneling across the insulating layers. At higher bias yielding current above ~1nA, transport is governed by Fowler-Nordheim (FN) tunneling¹⁸, while for direct tunneling near zero bias, the current is below the noise level (~1pA) for samples of this thickness. A zero-bias conductivity is measurable in thinner samples, however (see Supplementary Fig. S1). For CrI₃ and

CrCl₃, decreasing temperature lowers the current level for a given voltage, whereas CrBr₃ shows the opposite trend. In order to verify this, we additionally measured resistance with continuously changing temperature, and the results are shown in the corresponding insets in the bottom panel of Fig. 2. Here, a marked kink (or peak) was observed at the magnetic transition temperature (T_{AFM} or T_{FM}) for each device. By taking the derivative of these curves, we determined the critical temperatures more precisely to be 46K for CrI₃, 37K for CrBr₃, and 17K for CrCl₃ (see Supplementary Fig. S2). These temperatures are consistent with previous reports for bulk CrBr₃²⁵ and CrCl₃²⁶, although few-layer CrI₃ shows a slightly lower value than that for the bulk crystal (61K)²⁷, possibly due to different interlayer spin coupling and/or stacking between the two systems^{28, 29}. The abrupt change in tunnel resistance at the critical temperature arises from spontaneous exchange splitting of the CrX₃ conduction band^{30,31}. We shall later discuss the results for the valence band. Below T_{AFM} (T_{FM}), increasing (decreasing) resistance with decreasing temperature for CrI₃ and CrCl₃ (CrBr₃) indicates that the ground-state interlayer magnetic ordering is AFM (FM) between adjacent layers, as tunneling across filters with antiparallel (parallel) spins raises (lowers) the effective barrier height. Schematic illustrations of these effects are shown in the top panel of Fig. 2. These results are consistent with several recent studies of ultrathin CrX₃³²⁻³⁴.

The different ground-state interlayer spin ordering observed in these three materials will yield different phase transitions and TMR behavior upon application of a magnetic field, both of which can be measured in our device geometry. In Fig. 3a-c, we show voltage vs. temperature at constant current for the same three devices at several different fields applied perpendicular to the layers. We chose a small, 0.1nA current level in order to minimize the effects of Joule heating. Nevertheless, we found that measured transition temperatures did not change up to 100nA (Supplementary Fig. S3). In general, increasing magnetic field polarizes spins parallel to the field

direction. For CrI₃ and CrCl₃, the field decreases the resistance at low temperature as the interlayer AFM ground state is gradually destroyed, consistent with magneto-optical studies^{16, 21-23}. For CrBr₃, however, the low-temperature resistance is barely changed, since a spin-parallel, interlayer FM state has already formed in the ground state. Instead, the largest change occurs around the critical temperature. Here, increasing magnetic field stabilizes the parallel spin state, and so the voltage is decreased while the transition temperature into this state, T_P , is increased. In CrI₃ and CrCl₃, we observe that for intermediate magnetic fields, not only is T_P pushed to higher temperatures, but a second transition to an antiparallel interlayer spin state can be seen at temperatures below T_{AP} and decreases for increasing field. In the limit of zero field, T_P and T_{AP} approach T_{FM} and T_{AFM} , respectively, critical temperatures for the transition to *spontaneous* magnetic order. These net results are reproducible over several different samples (see Supplementary Fig. S4). We have additionally performed field-sweep measurements at several different temperatures (see Supplementary Fig. S5). The combined dataset allows us to obtain a field-temperature phase diagram for all three materials, as shown in Fig. 3d-f. In the spin schematics for the ground state, the easy axis is drawn to be out of plane for CrI₃ and CrBr₃, while it is in-plane for CrCl₃, as had been just recently demonstrated³²⁻³⁴.

A field-induced transition to the spin-parallel state should be accompanied by substantial TMR. We show I-V plots with and without a 5.5T perpendicular field for CrI₃ and CrCl₃ (insets of Fig 4a and b) and for CrBr₃ (see inset of Supplementary Fig. S6a) at 1.4K. When the field is applied, we generally observe clear TMR as the current is enhanced for any given voltage. For constant voltage biasing V , we define the TMR percentage between 0 and 5.5T as $\text{TMR} (\%) = \frac{I(5.5T,V) - I(0T,V)}{I(0T,V)} \times 100\%$ ²⁴, and have plotted these voltage-dependent values in the main panels of Fig. 4a, Fig. 4b, and Fig. S6a for CrI₃, CrCl₃, and CrBr₃, respectively. First, we notice that the

devices exhibit a noticeable asymmetry between negative and positive voltage. While we are unclear as to the precise origin of this effect, we note that there is an inherent asymmetry built into the device geometry as the top and bottom graphite layers are not identical. Different doping levels between the two will lead to different barrier heights and cause asymmetric I-V as our later analysis will show. Similar behavior was also observed in previous reports^{18, 19}. Nevertheless, at an optimized voltage level, we find that TMR at 1.4K reaches as high as $6 \times 10^5\%$ in CrI₃ and 1490% in CrCl₃ (Fig. 4a and b), whereas a much smaller TMR of $\sim 10\%$ was observed in CrBr₃ (Fig. S6), owing to the pre-formed, spin-parallel ground state. Overall, we attribute the larger TMR values to the high-quality interfaces naturally formed between the crystalline layers, as well as the sizable spin splitting of the electron bandstructure, which we shall discuss in detail below.

In order to determine the smallest magnetic field necessary to achieve the large TMR, we measured normalized current at the optimal voltage with continuously changing field. These results are shown in main panel of Fig. 4c. We observe that the TMR response for CrI₃ and CrCl₃ effectively saturates at 2T, the critical polarizing field for these two materials in the ground state³². Up to this field, however, the current for CrI₃ increases in discrete steps, while that for CrCl₃ increases continuously. This could be understood by the difference in magnetic anisotropy between the two^{31, 32}. Within the layers, CrI₃ exhibits the characteristics of a strong Ising ferromagnet with out-of-plane easy axis. A perpendicular field thus acts to flip the layers that are initially polarized in the opposite direction one by one. CrCl₃, on the other hand, has an in-plane easy axis, and so the same field smoothly rotates the spins until they are fully aligned. Finally, TMR in the CrBr₃ device is small and negligible up to 5.5T. We next repeated these measurements at many different temperatures and have plotted the TMR percentage for all three devices as a function of temperature in Fig. 4d. While both CrI₃ and CrCl₃ show decreasing TMR with increasing

temperature, CrBr₃ shows the opposite trend up to 40K, at which its maximum TMR is found to be ~200% (see also Supplementary Fig. S6b). In particular, the values for CrBr₃ and CrCl₃ cross at ~30K.

The contrasting TMR behavior in the three materials could be quantitatively explained by considering spin-dependent tunneling in the FN regime. Here, the current-voltage relation scales as $\ln\left(\frac{I_{\uparrow\downarrow}}{V^2}\right) \sim \frac{\Phi_{\uparrow\downarrow}^{3/2}(B)}{V}$, where $\Phi_{\uparrow\downarrow}(B)$ is the tunnel barrier for electrons of different spin in CrX₃ and is tunable by magnetic field. As the work function of few-layer graphene³⁵ is expected to be close to the electron affinity of CrX₃³⁶, the tunneling current is dominated by electron carriers. For CrI₃ and CrCl₃ in the anti-parallel ground state, electrons of both spins encounter a spatially modulated barrier with effective height $\Phi_{\uparrow,eff}^{AP} = \Phi_{\downarrow,eff}^{AP}$. In the spin-parallel state with $\geq 2T$ upward field, the barrier becomes uniform, with $\Phi_{\uparrow}^P < \Phi_{eff}^{AP} < \Phi_{\downarrow}^P$. The lower barrier for spin-up electrons yields an exponential rise in spin-filtered current, which manifests as large TMR. A schematic bandstructure outlining these quantities is shown in the inset of Fig. 4c. The spin-degenerate barrier in the paramagnetic state near the transition temperature, Φ^{PM} , is also shown, together with the exchange-induced gap, $E_{ex} = \Phi_{\downarrow}^P - \Phi_{\uparrow}^P = 2(\Phi^{PM} - \Phi_{\uparrow}^P)$. By fitting the current-voltage data to the FN formula at different magnetic field levels and temperatures, we are able to extract these various barrier heights. More detailed information about this process can be found in Supplementary Information: Section V. These quantities are summarized in Table 1 for all three compounds. In particular, CrI₃ shows larger TMR than CrCl₃ due to larger E_{ex} (lower Φ_{\uparrow}^P) relative to Φ_{eff}^{AP} . The exchange splitting decreases with increasing temperature and gradually disappears above T_{AFM} ¹⁸.

In contrast, for CrBr₃ at low temperature, increasing field has a negligible effect on the barriers since they are already split uniformly in the P state. The peak TMR in CrBr₃ starting in

the paramagnetic (PM) state near $T_{FM} \sim 40\text{K}$ then suggests a different mechanism. In order to explore this further, we have measured current vs. field at optimal voltage biasing for all three materials at their respective magnetic transition temperatures. In Fig. 5a, we show this dependence with current normalized to that at zero field. In all cases, current increases smoothly without saturation up to 14T, with CrI_3 showing the largest change, corresponding to a TMR value of 17000%.

At these temperatures, increasing magnetic field induces the splitting of Φ^{PM} , with $\Phi_{\uparrow}^P < \Phi_{\downarrow}^{PM} < \Phi_{\downarrow}^P$, also resulting in considerable TMR. We have further extracted E_{ex} as a function of magnetic field by performing full current-voltage measurements, and the results are plotted in Fig. 5b. For comparison, the respective exchange splitting in the ground state is marked as a dashed line. Relative to this value, at 14T the field-induced splitting at the transition temperature is already $\sim 82\%$ in CrI_3 , $\sim 85\%$ in CrBr_3 , and $\sim 87\%$ in CrCl_3 , all two orders of magnitude larger than the Zeeman energy ($\sim 1.7\text{meV}$ at 14T). This effect may be analogous to that observed in the colossal MR materials undergoing a PM insulator to FM metal transition, wherein the field suppresses the resistance caused by critical spin fluctuations or phase disorder¹⁴. This surprising result indicates that large exchange coupling can be induced in these materials at elevated temperatures even with moderate magnetic fields.

Finally, all the analysis of the electron barrier heights so far was carried out on devices using few-layer graphene electrodes with relatively low work function (4.42eV)³⁵. We have additionally investigated the spin splitting of the valence band in CrI_3 using few-layer NbSe_2 contacts with a higher work function ($\sim 5.9\text{eV}$)³⁷. The results are discussed in Supplementary Information: Section VI. Overall, the critical temperature and field remain similar; however, TMR is $\sim 10^4$ times lower ($\sim 70\%$), from which we estimate E_{ex} to be 2–3meV, consistent with theoretical

expectations³¹.

In summary, we have investigated the magnetic properties of all three chromium halides in the atomically thin limit by incorporating them in van der Waals tunnel junctions. We have systematically characterized both the ground state and field-driven phases as well as their TMR behavior with changing bias, temperature, thickness, and metal contact. While thicker samples with smaller work function graphene electrodes generally show higher TMR due to multiple spin filters of tunneling electrons acting in series, we find that the field range of the TMR response can be further tuned with temperature. Our work will have important implications for future devices utilizing these 2D materials.

Methods

Crystal synthesis. CrI₃ and CrCl₃ single crystals were grown by the chemical vapor transport method. We used a two-zone horizontal tube furnace. The temperature for source (growth) zones was gradually raised to 993 – 873K (823 – 723K) within 24 hours, and then held for 150 hours for actual growth. CrBr₃ single crystals was purchased from HQ graphene.

Device fabrication. Graphite (CoorsTek), h-BN (HQ graphene), CrI₃, CrBr₃, and CrCl₃ were exfoliated onto SiO₂(285nm)/Si chip within a nitrogen-filled glove box (Inert Pure LabHE, $P_{O_2}, P_{H_2O} < 0.1\text{ppm}$). By using a polymer-assisted pickup method reported previously³⁸, we sequentially stacked the structure of hBN/graphite/CrX₃/graphite/hBN in a home-built transfer setup inside the glove box, followed by transferring whole stack onto pre-patterned Au (40nm)/Ti (5nm) electrodes produced by conventional photolithography & lift-off methods and e-beam deposition. The overlapping area of graphite/CrX₃/graphite was set to be $\sim 10 \mu\text{m}^2$ for few-layer devices and $\sim 1 \mu\text{m}^2$ for bilayer devices. 1.4- to 7- nm-thick CrI₃ (2, 4, 8, and 10L), 1.3- to 7.8-nm-thick CrBr₃ (2, 8, 10, and 12L), and 1.2- to 9-nm-thick CrCl₃ (2, 8, 10, 12 and 15L) were used for fabrication. Graphite flakes were connected to pre-patterned electrodes and h-BN layers were used as protecting layers. Devices were stored inside the glovebox until they were loaded into the cryostat.

Acknowledgments

AWT acknowledges support from the US Army Research Office (W911NF-19-10267), an Ontario Early Researcher Award (ER17-13-199), and the Korea-Canada Cooperation Program through the National Research Foundation of Korea (NRF) funded by the Ministry of Science, ICT and Future

Planning (NRF-2017K1A3A1A12073407). G-XM acknowledges support from an NSERC Discovery grant (RGPIN-04178). This research was undertaken thanks in part to funding from the Canada First Research Excellence Fund. HCL acknowledges support from the National Key R&D Program of China (Grants No. 2016YFA0300504), the National Natural Science Foundation of China (No. 11574394, 11774423, 11822412), the Fundamental Research Funds for the Central Universities, and the Research Funds of Renmin University of China (RUC) (15XNLQ07, 18XNLG14, 19XNLG17).

Competing interests

The authors declare no competing interests.

Supporting Information

The Supporting Information is available free of charge on the ACS Publications website.

I-V characteristics for bilayer CrX₃ devices

Determination of magnetic transition temperature

Additional magnetotransport measurements for CrCl₃ and CrBr₃ devices

Temperature-dependent TMR of CrBr₃ device

Barrier height calculation

Magnetotransport for CrI₃ device using NbSe₂ electrodes

References

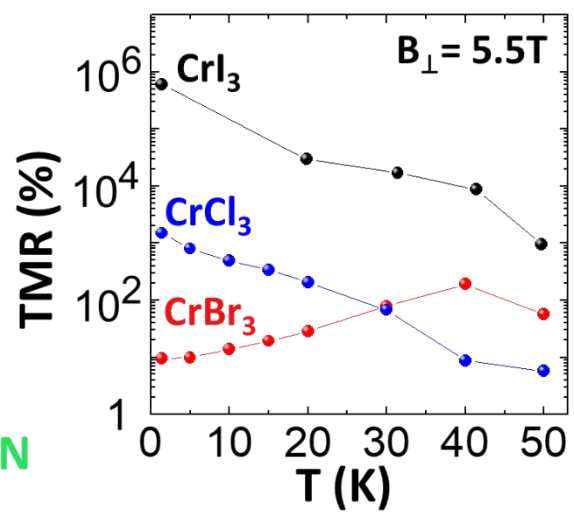
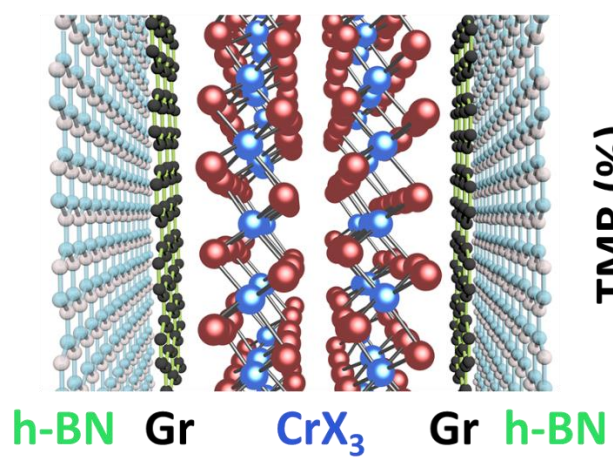
1. Wolf, S. A.; Awschalom, D. D.; Buhrman, R. A.; Daughton, J. M.; von Molnár, S.; Roukes, M. L.; Chtchelkanova, A. Y.; Treger, D. M., Spintronics: A Spin-Based Electronics Vision for the Future. *Science* **2001**, *294* (5546), 1488.
2. Žutić, I.; Fabian, J.; Das Sarma, S., Spintronics: Fundamentals and applications. *Rev. Mod. Phys.* **2004**, *76* (2), 323-410.
3. Ali, M. N.; Xiong, J.; Flynn, S.; Tao, J.; Gibson, Q. D.; Schoop, L. M.; Liang, T.; Haldolaarachchige, N.; Hirschberger, M.; Ong, N. P., *et al.*, Large, non-saturating magnetoresistance in WTe_2 . *Nature* **2014**, *514*, 205.
4. Moritomo, Y.; Asamitsu, A.; Kuwahara, H.; Tokura, Y., Giant magnetoresistance of manganese oxides with a layered perovskite structure. *Nature* **1996**, *380* (6570), 141-144.
5. Daughton, J. M., GMR applications. *J. Magn. Magn. Mater.* **1999**, *192* (2), 334-342.
6. Lenz, J. E., A review of magnetic sensors. *Proc. IEEE* **1990**, *78* (6), 973-989.
7. Keum, D. H.; Cho, S.; Kim, J. H.; Choe, D.-H.; Sung, H.-J.; Kan, M.; Kang, H.; Hwang, J.-Y.; Kim, S. W.; Yang, H., *et al.*, Bandgap opening in few-layered monoclinic MoTe_2 . *Nat. Phys.* **2015**, *11*, 482.
8. Wang, Y.; Wang, L.; Liu, X.; Wu, H.; Wang, P.; Yan, D.; Cheng, B.; Shi, Y.; Watanabe, K.; Taniguchi, T., *et al.*, Direct Evidence for Charge Compensation-Induced Large Magnetoresistance in Thin WTe_2 . *Nano Lett.* **2019**, *19*, 3969-3975.
9. Zhou, Q.; Rhodes, D.; Zhang, Q. R.; Tang, S.; Schönemann, R.; Balicas, L., Hall effect within the colossal magnetoresistive semimetallic state of MoTe_2 . *Phys. Rev. B* **2016**, *94* (12), 121101.
10. Luo, Y.; Li, H.; Dai, Y. M.; Miao, H.; Shi, Y. G.; Ding, H.; Taylor, A. J.; Yarotski, D. A.; Prasankumar, R. P.; Thompson, J. D., Hall effect in the extremely large magnetoresistance semimetal WTe_2 . *Appl. Phys. Lett.* **2015**, *107* (18), 182411.
11. Zhong, S.; Tiwari, A.; Nichols, G.; Chen, F.; Luo, X.; Sun, Y.; Tsen, A. W., Origin of magnetoresistance suppression in thin γ - MoTe_2 . *Phys. Rev. B* **2018**, *97* (24), 241409.
12. Wang, L.; Gutiérrez-Lezama, I.; Barreteau, C.; Ubrig, N.; Giannini, E.; Morpurgo, A. F., Tuning magnetotransport in a compensated semimetal at the atomic scale. *Nat. Commun.* **2015**, *6*, 8892.
13. Lee, Y. M.; Hayakawa, J.; Ikeda, S.; Matsukura, F.; Ohno, H., Effect of electrode composition on the tunnel magnetoresistance of pseudo-spin-valve magnetic tunnel junction with

a MgO tunnel barrier. *Appl. Phys. Lett.* **2007**, *90* (21), 212507.

14. Ramirez, A. P., Colossal magnetoresistance. *J. Phys. Condens. Matter.* **1997**, *9* (39), 8171-8199.
15. Gong, C.; Li, L.; Li, Z.; Ji, H.; Stern, A.; Xia, Y.; Cao, T.; Bao, W.; Wang, C.; Wang, Y., *et al.*, Discovery of intrinsic ferromagnetism in two-dimensional van der Waals crystals. *Nature* **2017**, *546*, 265-269.
16. Huang, B.; Clark, G.; Navarro-Moratalla, E.; Klein, D. R.; Cheng, R.; Seyler, K. L.; Zhong, D.; Schmidgall, E.; McGuire, M. A.; Cobden, D. H., *et al.*, Layer-dependent ferromagnetism in a van der Waals crystal down to the monolayer limit. *Nature* **2017**, *546*, 270-273.
17. Deng, Y.; Yu, Y.; Song, Y.; Zhang, J.; Wang, N. Z.; Wu, Y. Z.; Zhu, J.; Wang, J.; Chen, X. H.; Zhang, Y., Gate-tunable Room-temperature Ferromagnetism in Two-dimensional Fe₃GeTe₂. *Nature* **2018**, *563*, 94-99.
18. Kim, H. H.; Yang, B.; Patel, T.; Sfigakis, F.; Li, C.; Tian, S.; Lei, H.; Tsen, A. W., One million percent tunnel magnetoresistance in a magnetic van der Waals heterostructure. *Nano Lett.* **2018**, *18*, 4885-4890.
19. Song, T.; Cai, X.; Tu, M. W.-Y.; Zhang, X.; Huang, B.; Wilson, N. P.; Seyler, K. L.; Zhu, L.; Taniguchi, T.; Watanabe, K., *et al.*, Giant tunneling magnetoresistance in spin-filter van der Waals heterostructures. *Science* **2018**, *360*, 1214-1218.
20. Wang, Z.; Gutiérrez-Lezama, I.; Ubrig, N.; Kroner, M.; Taniguchi, T.; Watanabe, K.; Imamoğlu, A.; Giannini, E.; Morpurgo, A. F., Very Large Tunneling Magnetoresistance in Layered Magnetic Semiconductor CrI₃. *Nat. Commun.* **2018**, *9*, 2516.
21. Huang, B.; Clark, G.; Klein, D. R.; MacNeill, D.; Navarro-Moratalla, E.; Seyler, K. L.; Wilson, N.; McGuire, M. A.; Cobden, D. H.; Xiao, D., *et al.*, Electrical control of 2D magnetism in bilayer CrI₃. *Nat. Nanotech.* **2018**, *13*, 544-548.
22. Jiang, S.; Li, L.; Wang, Z.; Mak, K. F.; Shan, J., Controlling magnetism in 2D CrI₃ by electrostatic doping. *Nat. Nanotech.* **2018**, *13*, 549-553.
23. Jiang, S.; Shan, J.; Mak, K. F., Electric-field switching of two-dimensional van der Waals magnets. *Nat. Mater.* **2018**, *17* (5), 406-410.
24. Miao, G.-X.; Müller, M.; Moodera, J. S., Magnetoresistance in Double Spin Filter Tunnel Junctions with Nonmagnetic Electrodes and its Unconventional Bias Dependence. *Phys. Rev. Lett.* **2009**, *102* (7), 076601.
25. Tsubokawa, I., On the Magnetic Properties of a CrBr₃ Single Crystal. *J. Phys. Soc. Jpn.* **1960**, *15* (9), 1664-1668.

26. McGuire, M. A.; Clark, G.; Kc, S.; Chance, W. M.; Jellison, G. E.; Cooper, V. R.; Xu, X.; Sales, B. C., Magnetic behavior and spin-lattice coupling in cleavable van der Waals layered CrCl₃ crystals. *Phys. Rev. Mater.* **2017**, *1* (1), 014001.
27. McGuire, M. A.; Dixit, H.; Cooper, V. R.; Sales, B. C., Coupling of Crystal Structure and Magnetism in the Layered, Ferromagnetic Insulator CrI₃. *Chem. Mater.* **2015**, *27* (2), 612-620.
28. Sivadas, N.; Okamoto, S.; Xu, X. D.; Fennie, C. J.; Xiao, D., Stacking-Dependent Magnetism in Bilayer CrI₃. *Nano Lett.* **2018**, *18* (12), 7658-7664.
29. Jiang, P.; Wang, C.; Chen, D.; Zhong, Z.; Yuan, Z.; Lu, Z.-Y.; Ji, W., Stacking tunable interlayer magnetism in bilayer CrI₃. *Phys. Rev. B* **2019**, *99* (14), 144401.
30. Lado, J. L.; Fernández-Rossier, J., On the origin of magnetic anisotropy in two dimensional CrI₃. *2D Mater.* **2017**, *4* (3), 035002.
31. Zhang, W.-B.; Qu, Q.; Zhu, P.; Lam, C.-H., Robust intrinsic ferromagnetism and half semiconductivity in stable two-dimensional single-layer chromium trihalides. *J. Mater. Chem. C* **2015**, *3* (48), 12457-12468.
32. Kim, H. H.; Yang, B.; Li, S.; Jiang, S.; Jin, C.; Tao, Z.; Nichols, G.; Sfigakis, F.; Zhong, S.; Li, C., *et al.*, Evolution of interlayer and intralayer magnetism in three atomically thin chromium trihalides. *Proc. Natl. Acad. Sci. U.S.A.* **2019**, *116* (23), 11131-11136.
33. Klein, D. R.; MacNeill, D.; Song, Q.; Larson, D. T.; Fang, S.; Xu, M.; Ribeiro, R. A.; Canfield, P. C.; Kaxiras, E.; Comin, R., *et al.*, Giant enhancement of interlayer exchange in an ultrathin 2D magnet. **2019**, preprint at <https://arxiv.org/abs/1903.00002>.
34. Cai, X.; Song, T.; Wilson, N. P.; Clark, G.; He, M.; Zhang, X.; Taniguchi, T.; Watanabe, K.; Yao, W.; Xiao, D., *et al.*, Atomically Thin CrCl₃: An in-Plane Layered Antiferromagnetic Insulator. *Nano Lett.* **2019**, *19* (6), 3993-3998.
35. Leenaerts, O.; Partoens, B.; Peeters, F. M.; Volodin, A.; Van Haesendonck, C., The work function of few-layer graphene. *J. Phys. Condens. Matter.* **2016**, *29* (3), 035003.
36. Li, H.; Xu, Y.-K.; Lai, K.; Zhang, W.-B., The enhanced ferromagnetism of single-layer CrX₃ (X = Br and I) via van der Waals engineering. *Phys. Chem. Chem. Phys.* **2019**, *21*, 11949-11955.
37. Shimada, T.; Ohuchi, F. S.; Parkinson, B. A., Work Function and Photothreshold of Layered Metal Dichalcogenides. *Jpn. J. Appl. Phys.* **1994**, *33*, 2696-2698.
38. Wang, L.; Meric, I.; Huang, P. Y.; Gao, Q.; Gao, Y.; Tran, H.; Taniguchi, T.; Watanabe, K.; Campos, L. M.; Muller, D. A., *et al.*, One-Dimensional Electrical Contact to a Two-Dimensional Material. *Science* **2013**, *342* (6158), 614-617.

SYNOPSIS TOC



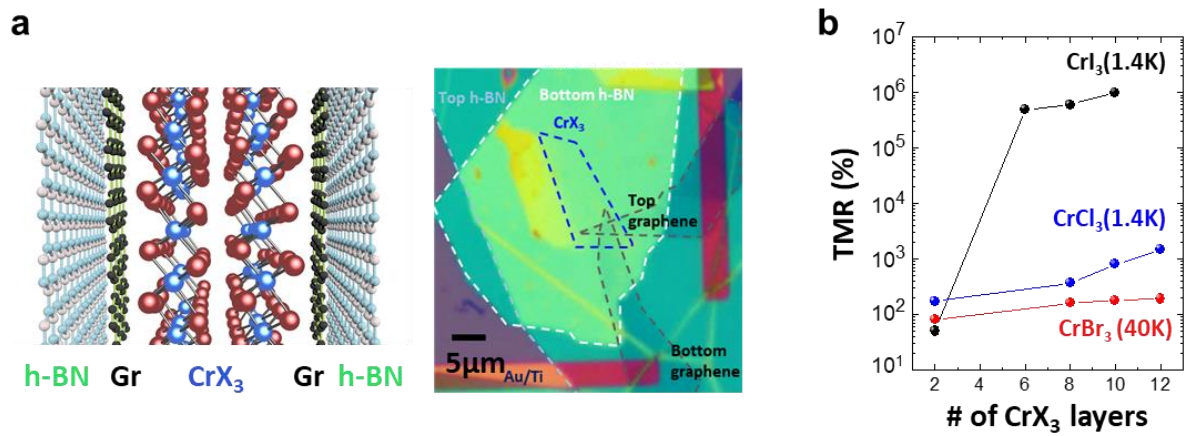


Figure 1. Van der Waals tunnel junctions incorporating ultrathin magnetic chromium trihalides. (a) Schematic illustration of the device (left) and an example optical image of a completed device with 2L CrI₃ (right). (b) Maximum TMR of CrX₃ as a function of the number of layers.

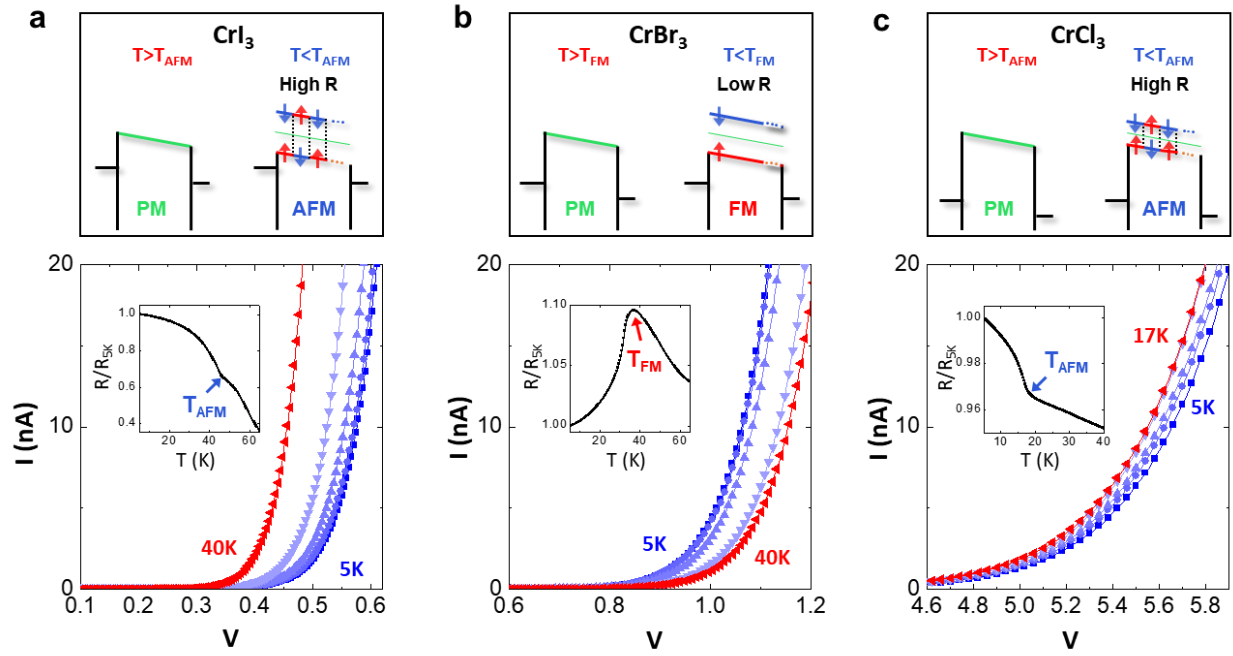


Figure 2. Temperature-dependent I-V measurement of (a) 8-layered CrI_3 (5, 10, 20, 30, and 40K), (b) 8-layered CrBr_3 (5, 10, 20, 30, and 40K), and (c) 15-layered CrCl_3 (5, 12, 14, 16, and 17K) at 0T. Insets show temperature-dependent, normalized d.c. resistance at 0T. Top panel shows respective, spin-dependent energy band diagrams of Gr/ CrX_3 /Gr tunnel junctions above and below the magnetic transition temperature.

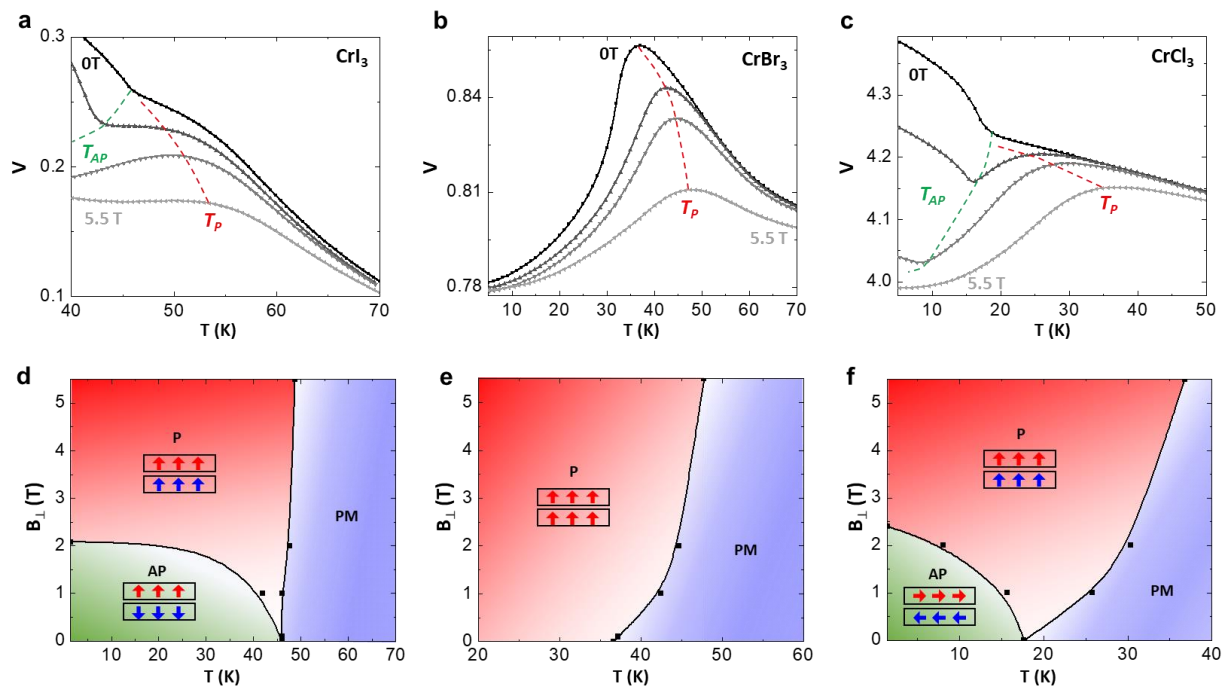


Figure 3. Tunneling probe of interlayer magnetic phases for three ultrathin chromium trihalides. (a) Voltage vs. temperature at 0.1 nA current biasing of a) 8-layer CrI_3 , (b) 8-layer CrBr_3 , and (c) 15-layer CrCl_3 for different B_{\perp} (0, 1, 2, and 5.5 T, in sequence from top) (d-f) Field-temperature phase diagram obtained from (a-c).

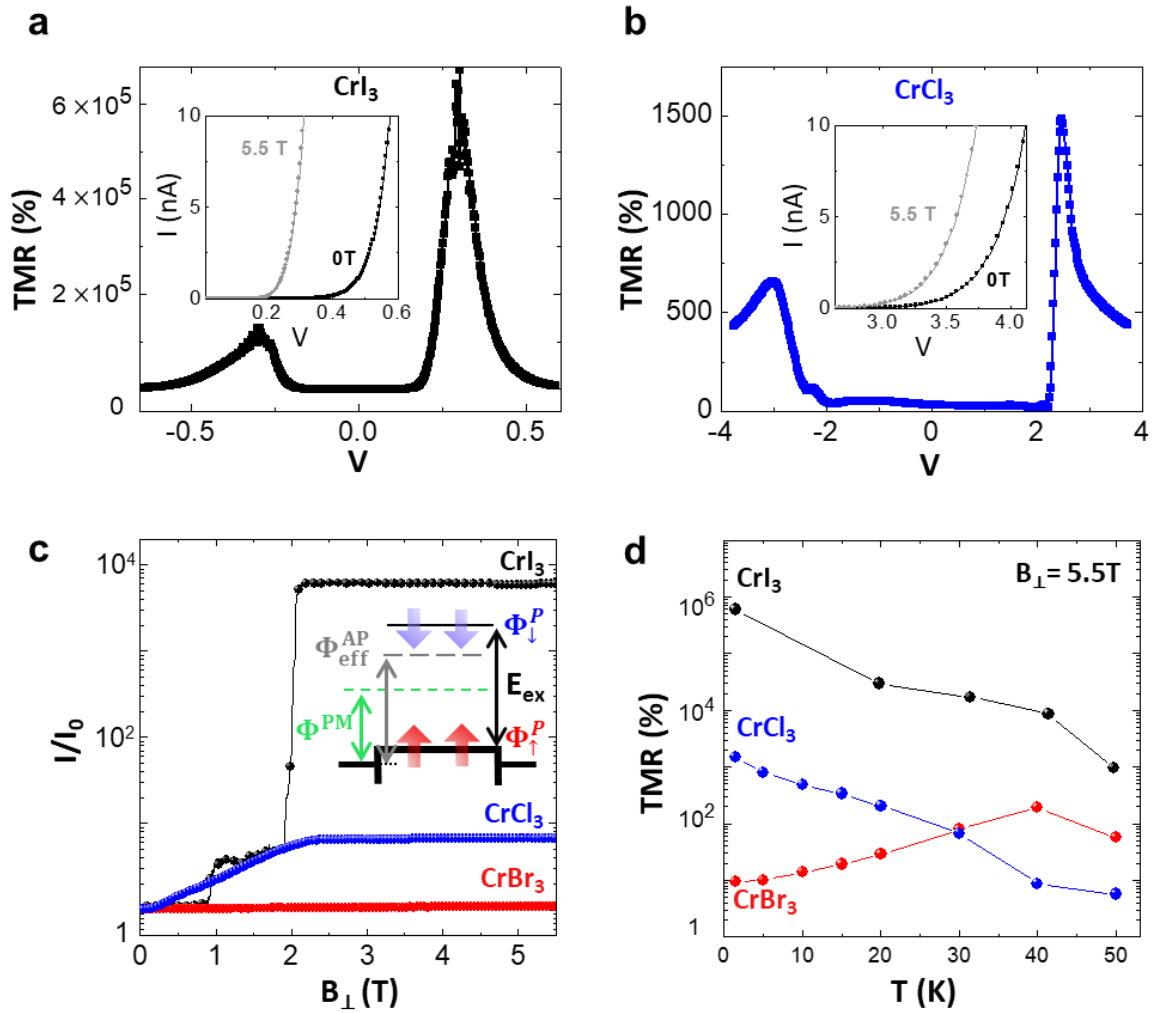


Figure 4. Tunnel magnetoresistance in three ultrathin chromium trihalides. TMR vs. voltage at 5.5T for in (a) 8L CrI₃ and (b) 12L CrCl₃ at 1.4K. Insets in (a) and (b) show full I-V characteristics at 0T and $B_{\perp} = 5.5$ T for the same devices. (c) Normalized tunnel current vs. perpendicular magnetic field at 1.4K for the same devices. Inset in (c) shows schematic illustration of spin-dependent energy band diagram for CrX₃ tunnel junction. (d) Temperature-dependent TMR at optimized voltage at $B_{\perp} = 5.5$ T.

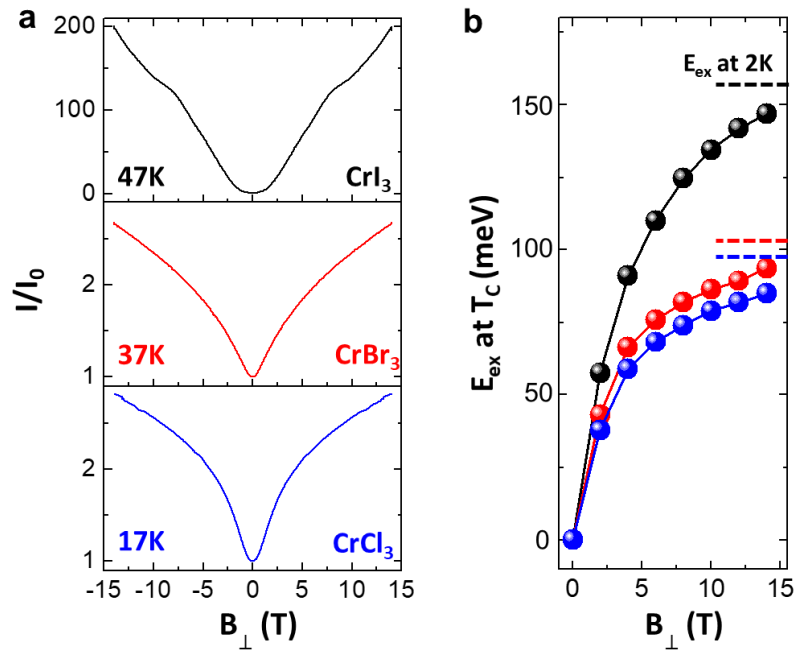


Figure 5. Non-saturating TMR behavior in few-layer CrX₃ at T_C. (a) field-dependent normalized current at optimized voltage (16L CrI₃: 0.33V, 10L CrBr₃: 1.3V, and 15L CrCl₃: 2.45V). (b) field-dependent exchange gap splitting for the same devices. Each dashed line indicates the spontaneous exchange splitting at 2K.

Table 1. Spin-dependent barrier height (in meV) between CrX₃ and few-layer graphene

	CrI₃	CrBr₃	CrCl₃
Φ^{PM}	227	538	943
$\Phi_{\text{eff}}^{\text{AP}} @ 1.4\text{K}$	273		964
$\Phi_{\uparrow}^P @ 1.4\text{K}$	159	477	909
$\Phi_{\downarrow}^P @ 1.4\text{K}$	295	599	977

Tailored tunnel magnetoresistance response in three ultrathin chromium trihalides

Hyun Ho Kim^{1*}, Bowen Yang¹, Shangjie Tian², Chenghe Li², Guo-Xing Miao¹,
Hechang Lei², and Adam W. Tsen^{1*}

¹*Institute for Quantum Computing, Department of Chemistry, Department of Physics and Astronomy, and Department of Electrical and Computer Engineering, University of Waterloo, Waterloo, Ontario N2L 3G1, Canada*

²*Department of Physics and Beijing Key Laboratory of Opto-electronic Functional Materials & Micro-Nano Devices, Renmin University of China, Beijing 100872, China*

*Correspondence to: hyun.kim@uwaterloo.ca, awtsen@uwaterloo.ca

This PDF file includes:

- I. I-V characteristics for bilayer CrX₃ devices
- II. Determination of magnetic transition temperature
- III. Additional magnetotransport measurements for CrCl₃ and CrBr₃ devices
- IV. Temperature-dependent TMR of CrBr₃ device
- V. Barrier height calculation
- VI. Magnetotransport for CrI₃ device using NbSe₂ electrodes

I. I-V characteristics for bilayer CrX₃ devices

In the main panel of Fig. S1, we show field-dependent I-V characteristics for three bilayer CrX₃ devices. The current is measurable down to zero bias. Maximum TMR in these samples is 50% for CrI₃, 80% for CrBr₃, and 170% for CrCl₃, all reduced from their thicker counterparts.

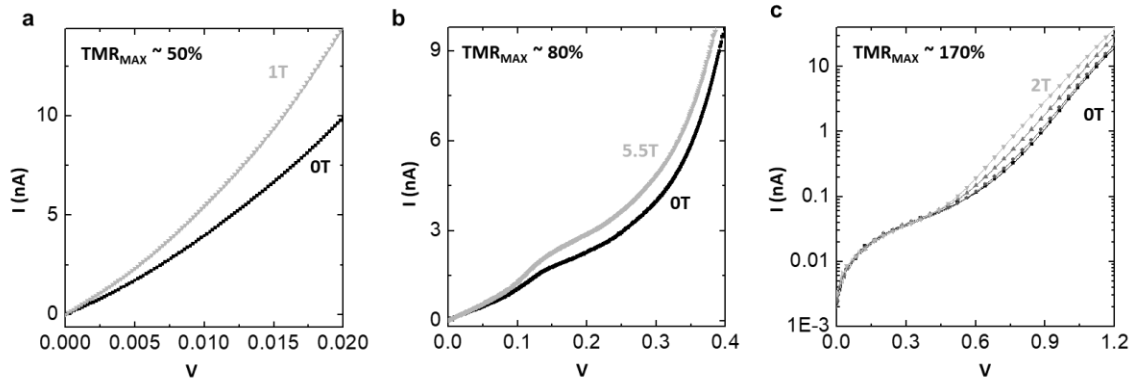


Figure S1. I-V characteristics for 2L (a) CrI₃, (b) CrBr₃, and (c) CrCl₃ devices. CrI₃ and CrCl₃ devices were measured at 1.4K and CrBr₃ device was measured at 40K.

II. Determination of magnetic transition temperature

The magnetic transition temperature of CrX_3 can be more precisely determined by taking the first or second derivatives of voltage vs. temperature (see Fig. S2). At T_{FM} , $dV/dT = 0$ in CrBr_3 , and at T_{AFM} , d^2V/dT^2 is peaked in CrI_3 and CrCl_3 .

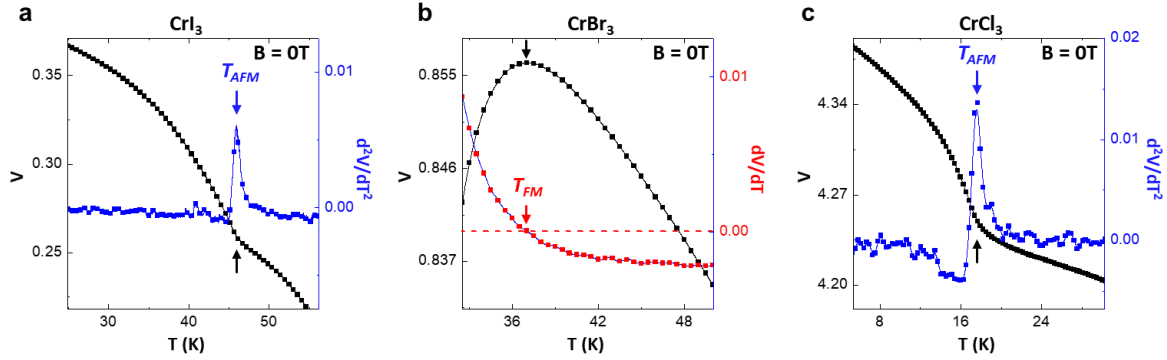


Figure S2. V vs. T plot and corresponding dV/dT or d^2V/dT^2 of (a) 8L CrI_3 , (b) 8L CrBr_3 , and (c) 15L CrCl_3 at 0 T.

We measured voltage vs. temperature at several different currents for few-layer CrI_3 to determine the significance of Joule heating on the measured transition temperature (see Fig. S3). T_{AFM} shows little change up to 100nA.

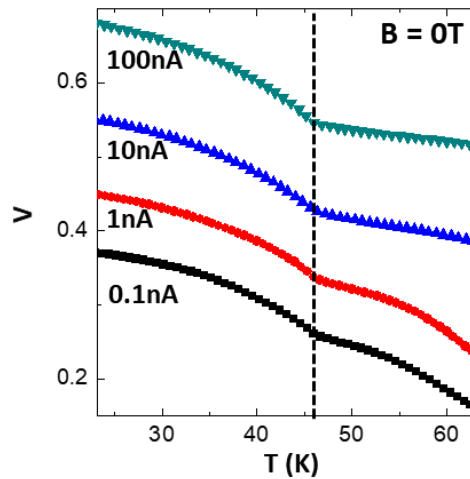


Figure S3. Voltage vs temperature of 8L CrI_3 for several different current biases.

III. Additional magnetotransport measurements for CrCl₃ and CrBr₃ devices

In Fig. S4, we show additional voltage vs. temperature measurements at different perpendicular fields (0, 1, 2, 5.5T) for 10, 12L CrCl₃ devices and 10, 14L CrBr₃ devices. In Fig. S5, we show voltage vs. perpendicular magnetic field at several different temperatures for 8L CrBr₃ and 15L CrCl₃, the same devices shown in Fig. 3. The combined data set allow for the construction of the phase diagrams in Fig. 3d-f.

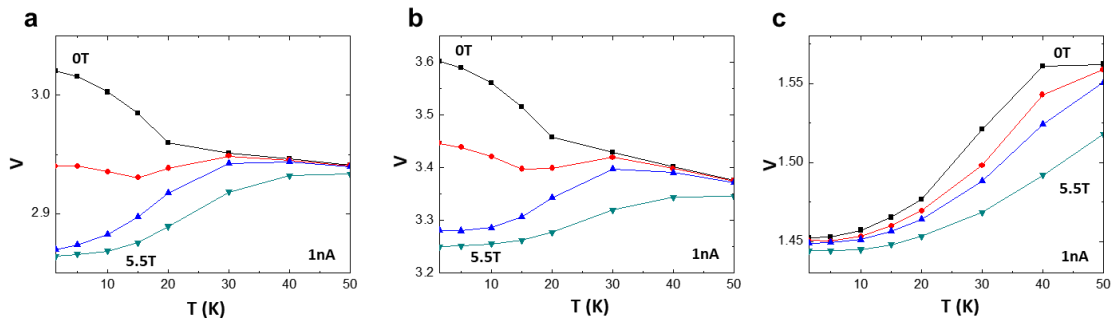


Figure S4. (a) Voltage vs temperature at 1nA for (a) 10L and (b) 12L CrCl₃ at $B_{\perp} = 0, 1, 2, 5.5$ T. Same for (c) 10L CrBr₃.

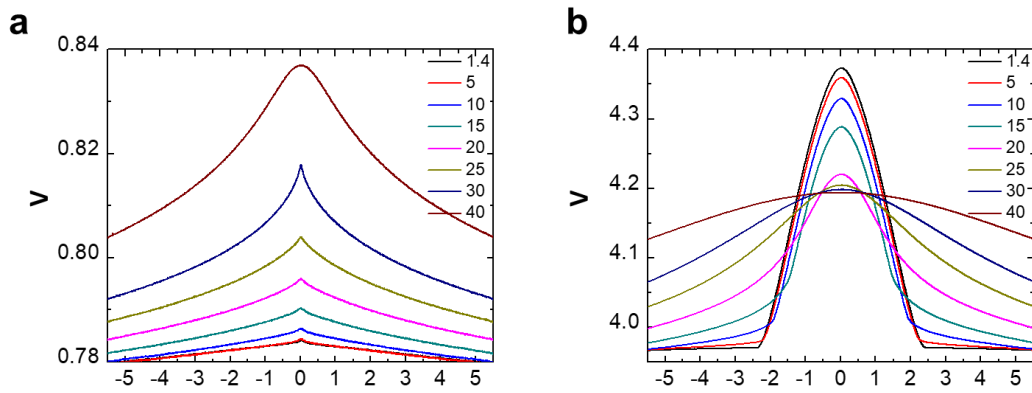


Figure S5. Voltage vs. perpendicular magnetic field at 1 nA for (a) 8L CrBr₃ and (b) 15L CrCl₃ at different temperatures.

IV. Temperature-dependent TMR of CrBr₃ device

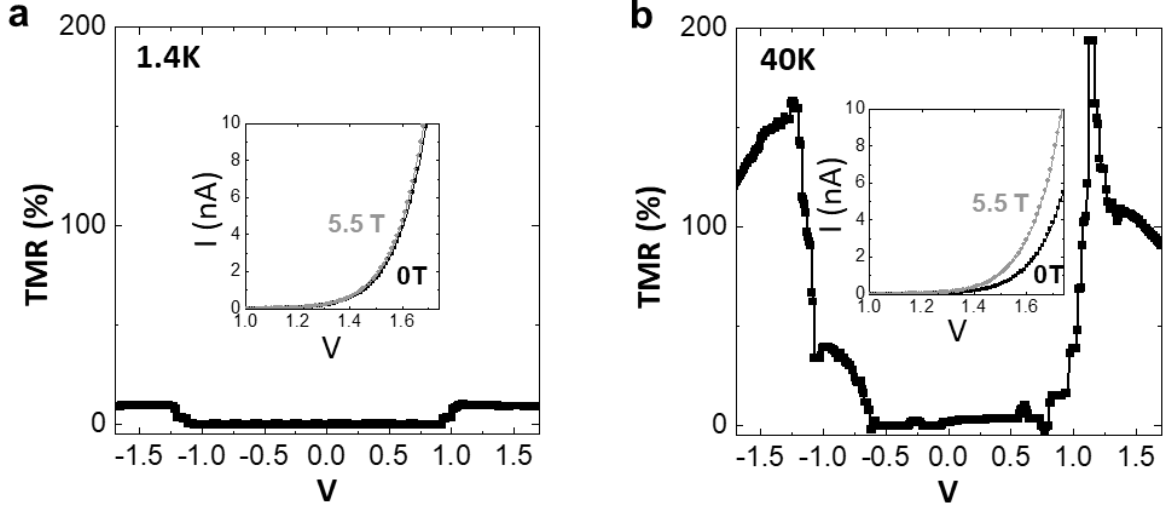


Figure S6. TMR vs. voltage at 5.5T for 12L CrBr₃ at (a) 1.4K and (b) 40K. Insets in (a) and (b) show I-V characteristics at 0T and $B_{\perp}=5.5$ T for the same devices.

V. Barrier height calculation

We calculated the spin-dependent barrier heights of CrX₃ devices using the Fowler-Nordheim (FN) current-voltage relation:

$$I \sim \frac{V^2}{\Phi} \exp\left(-\frac{4d\sqrt{2m}\Phi^3}{3\hbar eV}\right),$$

where e is electronic charge, d is the CrX₃ thickness, m is the effective electron mass (estimated to be the free-electron mass), \hbar is the Planck's constant, and Φ is the barrier height between the graphene electrode and CrX₃. We can linearize this relation by plotting $\ln\left(\frac{I}{V^2}\right)$ vs. $\frac{1}{V}$, and extracting Φ from the slope. This is shown in Fig. S7 for all three CrX₃.

The various barrier heights are obtained under different field and temperature conditions.

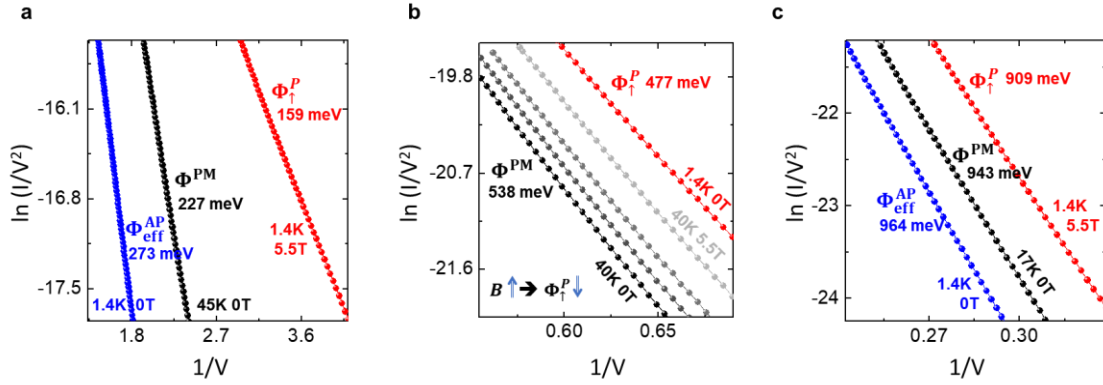


Figure S7. $\ln(I/V^2)$ vs. $1/V$ for (a) 8L CrI₃, (b) 12L CrBr₃, and (c) 12L CrCl₃. Φ is determined by the slope. The magnetic field levels for the traces in (b) are 0, 1, 2, 5.5T from black to gray.

VI. Magnetotransport for CrI₃ device using NbSe₂ electrodes

We additionally fabricated a CrI₃ device with high work function NbSe₂ (5.9eV) electrodes to investigate the spin-dependent current for hole transport (h-BN/NbSe₂/CrI₃/NbSe₂/h-BN). The results show that the critical polarizing field remains similar to that for devices using graphene electrodes, but with $\sim 10^4$ times lower TMR percentage, as shown in Fig. S8.

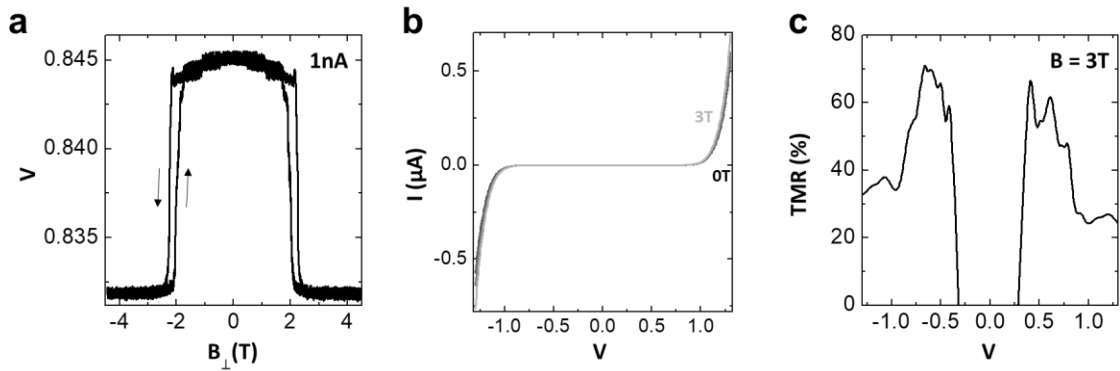


Figure S8. Magnetotransport results for NbSe₂/CrI₃/NbSe₂ tunnel junction device at 1.8K. The thickness for each material was measured to be ~ 10 nm. (a) Field-dependent voltage measurement at 1nA. (b) I-V plots from 0 to 3T, in sequence from black to grey. (c) voltage-dependent TMR at 3T.